

# PCCP

Accepted Manuscript



This is an *Accepted Manuscript*, which has been through the Royal Society of Chemistry peer review process and has been accepted for publication.

*Accepted Manuscripts* are published online shortly after acceptance, before technical editing, formatting and proof reading. Using this free service, authors can make their results available to the community, in citable form, before we publish the edited article. We will replace this *Accepted Manuscript* with the edited and formatted *Advance Article* as soon as it is available.

You can find more information about *Accepted Manuscripts* in the [Information for Authors](#).

Please note that technical editing may introduce minor changes to the text and/or graphics, which may alter content. The journal's standard [Terms & Conditions](#) and the [Ethical guidelines](#) still apply. In no event shall the Royal Society of Chemistry be held responsible for any errors or omissions in this *Accepted Manuscript* or any consequences arising from the use of any information it contains.

# Atomic scale mobility of the volatile fission products Xe, Kr and I in cubic SiC

M.W.D. Cooper<sup>a,b</sup>, S. Kelly<sup>a,b</sup>, M. Bertolus<sup>b</sup>

<sup>a</sup>*Department of Materials, Imperial College London, London, SW7 2AZ, UK*  
<sup>b</sup>*CEA, DEN, DEC, Centre de Cadarache, 13108 Saint-Paul-Lez-Durance, France*

---

## Abstract

The migration barriers for the vacancy-assisted migration of fission products in 3C-SiC are reported and analysed in the context of the five frequency model, which enables one to calculate an effective diffusion coefficient from elementary mechanisms. Calculations were carried out using the nudged elastic band method (NEB) with interatomic forces determined from density functional theory (DFT). Justification for treating vacancy-assisted fission product migration as limited to the FCC carbon sublattice is based on the stability of carbon vacancies, unfavourable silicon vacancy formation and the accommodation of fission products on the carbon sublattice. Results show that for most Fermi levels within the band gap the activation energy for I exceeds that of Xe which exceeds that of Kr. Results also indicate that activation energies are higher near the conduction edge, thus, implying that enhanced fission product retention can be achieved through n-type doping of 3C-SiC, which limits the availability of the migration mediating carbon vacancies.

*Keywords:* Silicon Carbide, Fission Products, Diffusion, Density Functional Theory

---

## 1. Introduction

Silicon carbide (SiC) exhibits a very high melting point and good chemical stability making it suitable for high temperature applications. In particular, as a wide band gap semiconductor, it has been touted for applications in high temperature electronic devices [1] and is envisaged as an alternative to Si. Furthermore, it has a low neutron capture cross section making it an interesting candidate material in fission and fusion reactors [2, 3]. Low fission product mobility in SiC makes it a prime candidate material for a barrier in advanced high temperature reactor designs. For example, the tristructural-isotropic (TRISO) particle fuel design employs SiC in this role [4].

A significant body of work has been undertaken to study the release of radiologically important fission products from nuclear fuel. For example, rare gas fission products, Xe and Kr, are highly insoluble in the UO<sub>2</sub> matrix and are released from the fuel in significant quantities [5–10]. Similarly, highly volatile fission products, such as I and Cs, rapidly migrate out of the host UO<sub>2</sub> matrix [11, 12]. Therefore, these fission products can provide a particular problem for retention and must be isolated through a barrier layer. The mobility of fission products in SiC has been studied experimentally [4, 13–16] and atomic scale simulations can be employed to develop a fundamental understanding of the underlying mechanisms. Density functional theory (DFT) has

---

*Email addresses:* [mwdc09@gmail.com](mailto:mwdc09@gmail.com) (M.W.D. Cooper), [marjorie.bertolus@cea.fr](mailto:marjorie.bertolus@cea.fr) (M. Bertolus)

been successfully applied to the investigation of defect behaviour in a number of nuclear materials [17–19]. SiC exhibits a large number of polytypes, the most common being the cubic 3C- and the two hexagonal 4H- and 6H-SiC structures. The 3C-SiC structure is simpler to model, while most experimental results have been obtained on 6H-SiC. Wiktor *et al.* [20] have shown that the extrapolation of the formation energies of point defects obtained in 3C-SiC to the gap of the 6H structure is a good approximation, especially for carbon defects.

In DFT [20–24] and the GW [25] approximation carbon vacancies are predicted to be the most stable intrinsic defects in SiC. Unlike GW [25, 26] or DFT using hybrid functionals [27], LDA and GGA DFT calculations [20–24] significantly underestimate the band gap. This leads to errors when investigating defect charge states and care must be taken when using standard DFT techniques for Fermi levels between the DFT conduction edge and the experimental conduction edge. These problems are highlighted by Bruneval and Roma [25, 26] where LDA defects energies are compared to GW defects energies over the full experimental band gap. Nonetheless they show that conventional DFT provides a good description of defect energies and charge states within the theoretical band gap, especially for the carbon vacancy [25]. Furthermore, if one considers Fermi levels relative to the theoretical band gap predicted by a given method, similar trends are shown for the charge states and formation energies of defects for GW and DFT [25, 26]. Therefore, DFT energies as a function of the Fermi level should be considered relative to the size of the band gap.

The results of Wiktor *et al.* [20], which used a similar methodology to that reported here, indicated that the carbon vacancy is in the +2 charge state over nearly the full theoretical band gap (1.38 eV), although if the Fermi level is near the conduction edge the neutral carbon vacancy was predicted to be favourable. Previously Rabone and Kovács [28], Bertolus *et al.* [21] and Charaf-Eddin and Pizzagalli [29] used DFT to investigate the incorporation of a number of fission products into neutral defects of SiC, including Xe, Kr and I. The substitution of these fission products onto the carbon sublattice was widely predicted to be very significantly more favourable than as an interstitial or on the Si sublattice. Similarly, Roma *et al.* [30] identified that Pd is preferentially accommodated on carbon sublattice either as a +2 or a neutral defect. Furthermore, the migration of Pd in SiC was also predicted to be restricted to vacancy-assisted migration on the FCC carbon sublattice when vacancies are present [31]. Alternatively, Ti, V, Nb, Cr, Mo and W have been predicted by Ivády *et al.* [32] to be favourably accommodated at the silicon vacancy in 3C-SiC or asymmetrically at a neutral Si-C divacancy in 4H- or 6H-SiC.

Here we investigate the mobility of Xe, Kr and I in 3C-SiC from their stable sites on the carbon sublattice by assuming a vacancy-assisted migration mechanism like that of Roma *et al.* [30]. This is justified because i) the most stable sites for these fission products are on the carbon sublattice, ii) the carbon vacancy is several orders more abundant than the silicon vacancy [33] and, furthermore, iii) over the full band gap of 3C-SiC the highly unfavourable and metastable silicon vacancy is predicted to be converted to a carbon vacancy  $C_{Si}$ -antisite complex (see Figure 1) [20, 33]. Additionally, although neutral Si-C divacancies are predicted to be an important defect in 4H-SiC [32, 34], the neutral C-C divacancy has been calculated to be 0.38 eV more stable than the neutral Si-C divacancy in 3C-SiC [21]. However, the formation energies for the Si-C and C-C divacancies will be considered for Fermi levels across the full band gap to rule out the involvement of the Si sublattice in the diffusion mechanism. For a more detailed representation of experiment, where hexagonal phases are common, Si-C divacancies should be considered, however this is beyond the scope of this work.

These assumptions allow an analysis of fission product mobility that is based on the five frequency model for vacancy-assisted diffusion on the FCC carbon sublattice of 3C-SiC. The regimes over which diffusion occurs via the +2 or neutral carbon vacancy are also discussed.

## 2. Methodology

### 2.1. Calculation parameters

All DFT calculations were carried out using the projector augmented wave (PAW) method [35, 36] as implemented in the Vienna *ab initio* Simulation Package (VASP) [37–39] with a plane wave cut-off energy of 600 eV. For carbon the  $2s$  and  $2p$  levels are treated as valence states (and level  $1s$  is included in the core region), whereas for silicon  $3s$  and  $3p$  are considered to be valence states (and the  $1s$ ,  $2s$  and  $2p$  levels constitute the core region). The parametrisation of Perdew, Burke and Ernzerhof (PBE) [40] for the Generalised Gradient Approximation (GGA) was used to describe the exchange-correlation interactions. Defect calculations were carried out on supercells of  $3 \times 3 \times 3$  sphalerite unit cells of SiC (216 atoms) with spin polarisation and no conservation of symmetry. The Brillouin zone was sampled using a  $2 \times 2 \times 2$  k-point mesh generated using the Monkhorst-Pack scheme [41]. Electron relaxation was optimised in reciprocal space with force and total energy convergence criteria of  $10^{-8}$  eVÅ $^{-1}$  and  $10^{-8}$  meV respectively. The perfect crystal properties predicted here are compared to experimental results in Table 1, showing a good agreement. Similar calculation parameters were used previously by Wiktor *et al.* [20] to determine positron lifetimes and the results showed a strong agreement with experiment. In addition, the insertion of Kr and Xe in SiC is correctly described using the PBE functional [21].

The formation energy of a charged defect was calculated by:

$$E_F = E_{tot}(V_{X,q}) - n_C \mu_{SiC}^{bulk} - (n_{Si} - n_C) \left[ \mu_{Si}^{bulk} + \frac{1}{2} \Delta H_f(\text{SiC}) \right] + q(E_{VBM} + \mu_e) \quad (1)$$

where  $E_{tot}$  is the energy of the defective supercell,  $\mu_{SiC}^{bulk}$  is the energy per SiC pair in the bulk, the energy per atom in bulk Si is  $\mu_{Si}^{bulk}$ . The Fermi level is given by  $\mu_e$  and  $E_{VBM}$  is the energy of the valence band maximum. The formation enthalpy of SiC,  $\Delta H_f(\text{SiC})$ , is given by:

$$\Delta H_f(\text{SiC}) = \mu_{SiC}^{bulk} - \mu_{Si}^{bulk} - \mu_C^{bulk} \quad (2)$$

where  $\mu_C^{bulk}$  is defined as the energy of a carbon atom within the diamond structure.

One issue with using the supercell approach for charged defects is the unphysical system charge that arises due to periodic boundary conditions. A charge neutralising background jellium must, therefore, be used [42–44]. However, defect energies must be adjusted according to the interaction energy of a periodically repeating system containing a point charge,  $q$ , with the neutralising background jellium, as defined by the Madelung energy [42, 43]:

$$\Delta E_{el}(q) = \frac{\alpha q^2}{2\epsilon L} \quad (3)$$

where  $\alpha$  is the Madelung constant ( $\alpha = 1.6381$  for 3C-SiC),  $\epsilon$  is permittivity of the medium and  $L$  is the supercell size length.  $\epsilon$  and  $L$  are defined from the geometry optimised perfect cell (Table 1). To calculate the additional potential correction term  $\Delta V$  the method of Taylor and Bruneval [45] is used, such that:

$$\Delta V = \langle v_{KS}^{bulk} \rangle - \langle v_{KS}^{defect} \rangle \quad (4)$$

where  $\langle v_{KS}^{bulk} \rangle$  and  $\langle v_{KS}^{defect} \rangle$  are the averaged Kohn-Sham potentials for the perfect and defective supercells respectively.

Migration barriers are calculated using the nudged elastic band (NEB) method [46] in conjunction with the same DFT parameters described above. For each NEB calculation the initial and final stable configurations of a given transition are determined using geometry optimisation.

Based on the linear interpolation of the initial and final atomistic configurations an initial guess of the lowest migration pathway, which is then minimised, is made at five discrete points. There are, as such, seven images of the lowest energy migration pathway including the initial and final configurations.

## 2.2. Five Frequency Model

Based on the justifications given in section 1 it is assumed that fission product migration is restricted to the FCC carbon sublattice. The five frequency model governing vacancy mediated impurity diffusion on an FCC lattice assumes that the second nearest neighbour distance is great enough so the vacancy-impurity binding is very low and can be neglected beyond this distance [47]. Therefore diffusion can be broken down into five constituent individual jump frequencies [48, 49]:

- $w_0$  - vacancy-atom exchange rate in the host material. Vacancy migration in the bulk whereby the bulk is defined as any jump not involving the first nearest neighbour site with respect to the impurity. In Figure 2  $w_0$  is represented by the blue arrow between the second and third nearest neighbour positions on the carbon sublattice.
- $w_1$  - rotation rate of the impurity-vacancy pair. The jump of a vacancy around the impurity between two first nearest neighbour sites, as represented by the yellow arrow in Figure 2.
- $w_2$  - impurity-vacancy exchange rate. The jump of the impurity into a vacancy that is occupying a first nearest neighbour site, as indicated by the red arrow in Figure 2.
- $w_3$  - dissociation rate of the impurity-vacancy pair. The jump of the vacancy from a first nearest neighbour position to a second nearest neighbour site. The purple arrow in Figure 2 represents dissociation.
- $w_4$  - association rate of the impurity-vacancy pair. Vacancy migration from a second nearest neighbour position into a first nearest neighbour site with respect to the impurity as indicated by the green arrow in Figure 2.

Each of the above jump frequencies,  $w_i$ , has an associated attempt frequency,  $v_i$ , and energy barrier,  $E_i$ , such that:

$$w_i = v_i \cdot \exp\left(\frac{-E_i}{k_B T}\right) \quad (5)$$

where  $k_B$  is the Boltzmann constant and  $T$  is the temperature. Generally, impurity diffusivity,  $D$ , can be described by:

$$D = \frac{1}{6} f \alpha^2 p v_2 \cdot \exp\left(\frac{-E_2}{k_B T}\right) \quad (6)$$

where  $\alpha$  is the jump distance for the vacancy-impurity exchange and  $p$  is the probability of finding a vacancy in a first nearest neighbour site with respect to the impurity, which can be expressed as follows:

$$p = N \cdot \exp\left(\frac{-(E_f + E_B)}{k_B T}\right) \quad (7)$$

where  $E_f$  is the bulk vacancy formation energy,  $E_B$  is the impurity-vacancy binding energy and  $N$  is the number of first nearest neighbour sites with respect to the impurity ( $N = 12$ ). In the absence of interaction beyond the first nearest neighbour, the binding energy can be calculated by  $E_B = E_4 - E_3$ . As such, if the vacancy and impurity attract ( $E_B < 0$ ) the probability of finding a vacancy in a first nearest neighbour site is enhanced with respect to the bulk concentration.

Equation 8 shows that the correlation factor,  $f$ , as a function of  $w_1$ ,  $w_2$ ,  $w_3$  and the escape probability,  $\frac{7F_3}{2}$  [48]:

$$f = \frac{w_1 + 7F_3w_3/2}{w_1 + w_2 + 7F_3w_3/2} \quad (8)$$

Although an explicit form of the escape probability,  $\frac{7F_3}{2}$ , is given in reference [48], the results of NEB calculations presented later show that for all cases studied here the association rate,  $w_4$ , far exceeds that of bulk vacancy migration,  $w_0$ . Consequently, every time the vacancy dissociates from the impurity it rapidly re-associates and the escape probability,  $\frac{7F_3}{2}$ , tends to one so that:

$$f = \frac{w_1 + w_3}{w_1 + w_2 + w_3} \quad (9)$$

Therefore, in conjunction with strong vacancy-impurity binding, whereby  $w_1 \gg w_3$ , this relationship can be further simplified to:

$$f = \frac{w_1}{w_1 + w_2} \quad (10)$$

The migrating species can, as such, be treated as a bound impurity-vacancy pair with some special cases discussed below:

- a) if  $w_1 \gg w_2$  vacancy migration around the impurity is significantly greater than impurity-vacancy exchange. This effectively randomises the position of the vacancy with respect to the impurity before the impurity jumps into the vacant site. As such,  $f \rightarrow 1$  in equation 10, so that the impurity diffusivity is expressed as:

$$D = 2\alpha^2 v_2 \exp\left(\frac{-(E_2 + E_f + E_B)}{k_B T}\right) \quad (11)$$

- b) if  $w_2 \gg w_1$  the impurity-vacancy exchange rate is far greater than the other jump frequencies. Consequently, the motion of the impurity is highly correlated as it 'rattles' back and forth between two adjacent lattice sites. Therefore, equation 10 gives  $f \rightarrow \frac{w_1}{w_2}$  and by assuming all attempt frequencies ( $v_i$ ) are approximately equal to the Debye frequency the impurity diffusivity is expressed as:

$$D = 2\alpha^2 v_1 \exp\left(\frac{-(E_1 + E_f + E_B)}{k_B T}\right) \quad (12)$$

Long range diffusion is, therefore, limited by the ability of the vacancy-impurity pair to reconfigure by rotation ( $w_1$ ).

- c) if  $w_2 \approx w_1$  there is a combined correlated impurity-vacancy exchange/rotation mechanism, whereby  $f \rightarrow \frac{1}{2}$  and the diffusivity is expressed as:

$$D = \alpha^2 v_{1=2} \exp\left(\frac{-(E_{1=2} + E_f + E_B)}{k_B T}\right) \quad (13)$$

This work is concerned firstly with identifying the stable configurations associated with the five frequency model and then determining all migration barriers between these configurations ( $E_0$ ,  $E_1$ ,  $E_2$ ,  $E_3$ ,  $E_4$  and  $E_5$ ). Based on the special cases, i)-iii), outline above an analysis of the vacancy-assisted migration mechanisms for Xe, Kr and I migration in cubic SiC is given.

### 3. Results and discussion

#### 3.1. Formation energies and charge states

Formation energies are reported as a function of  $\mu_e$  in Figure 3 for a carbon vacancy and a first nearest neighbour carbon-carbon divacancy. Values are reported for Fermi levels between the experimental valence edge and conduction edge (2.39 eV), however, as the computational band gap is just 1.38 eV one must consider the defect energies in the upper limit of the theoretical band gap as commensurate with Fermi levels near the experimental conduction band (see section 1). This is supported by comparison with GW results [26], which show similar trends from  $0 < \mu_e < 2.39$  to those predicted by DFT from  $0 < \mu_e < 1.38$ . Despite the qualitative agreement between DFT and GW over their respective theoretical band gaps, it is possible for DFT to underestimate the defect energies near the theoretical conduction band and our conclusions should be qualitative in nature. Figure 3 indicates that over the calculated band gap the +2 charged supercell dominates for both the single carbon vacancy and the carbon-carbon divacancy. However, near the conduction edge the neutral supercell becomes favourable. It is only when the Fermi level significantly exceeds that of the computational conduction edge that any negative charge states exist for carbon vacancy type defects. Comparison with GW [25] indicates that these charge states are unphysical and are omitted from further analysis using the five frequency model. Furthermore, Figure 3c) shows that for all Fermi levels within the theoretical band gap of 3C-SiC the C-C divacancy is more stable than Si-C divacancy. As such, the latter is discounted from further consideration in the diffusion mechanism. Note that this is contrary to previous work on 4H-SiC [32, 34], where the Si-C divacancy must be taken into account.

As for the carbon vacancies, a Xe impurity occupying a carbon site,  $\text{Xe}_C$ , is also dominated by the +2 charged supercell over the full calculated band gap (see Figure 4a). Alternatively, if the xenon impurity has an additional carbon vacancy in a first nearest neighbour carbon site the neutral charge state becomes favourable near the conduction edge (see Figure 4b). Again one only encounters alternative charge states when  $\mu_e$  is significantly greater than 1.38 eV.

Due to similar chemistry the Kr formation energies are very similar to that of Xe; the +2 charged defects dominate over the the full computational band gap (see Figure 5). However, if a carbon vacancy occupies a first nearest neighbour carbon site to the Kr impurity the neutral supercell becomes favourable near the near the computational conduction edge.

Figure 6 shows that the accommodation of I at a carbon site is also dominated by the the +2 charge state over nearly the full theoretical band gap. If the first nearest neighbour carbon site with respect to the impurity is vacant the +2 supercell is also more favourable over a broad range of Fermi levels. However, near the top of the theoretical band gap alternative valence states become favourable.

For all defects studied here that are involved in the five-frequency model on the carbon sublattice it is clear that the +2 charge state is dominant over a broad range of the computational band gap. However, the neutral charge state is important near the conduction edge for the formation of the migration mediating carbon vacancies as well as for the accommodation of the noble gases Xe and Kr. Therefore, all migration barriers involved in the five-frequency model will be examined in both the neutral and the +2 charged supercells.

#### 3.2. Migration barriers of the five-frequency model

The stable configurations calculated in section 3.1 define the initial and final configurations for  $E_0$ ,  $E_1$  and  $E_2$ . Whilst the initial configuration for  $E_3/E_4$  is also given by the impurity-vacancy first nearest neighbour configuration, the final configuration was calculated by energy minimisation of the impurity-vacancy second nearest neighbour configuration. Using these initial and final configurations the NEB method was used to calculate the energy barriers.

For summary the energy barriers associated with the five frequency model (i.e.  $E_{0-4}$ ) for I, Xe and Kr are shown in Table 2. The charge neutral and +2 supercell cases are both reported. Bockstedte *et al.* [50] calculated  $E_0$  values of 3.5 eV and 5.2 eV for the neutral and +2 case respectively, in good agreement with our results. One should note that in all cases  $E_4 < E_0$  (or  $w_4 \gg w_0$ ) so that if the vacancy overcomes the binding energy with the impurity to reach a second nearest neighbour site it is highly likely that it will re-associate with the impurity rather than migrate into the bulk. Additionally, all cases exhibit strong binding energies ( $E_3 > E_4$ ) in line with the limiting cases discussed at the end of section 2.2. Therefore, the relative heights of the  $E_1$  and  $E_2$  energy barriers determine the specific limiting case.

Figure 7 shows the  $E_1$  and  $E_2$  barriers associated with the five frequency model for Xe in the neutral supercell regime (green), indicating  $E_1 > E_2$ . Consequently, the extremely high dependency of the jump frequency on the energy barrier (equation 5) dictates that  $w_2 \gg w_1$ . The diffusivity is therefore determined by equation 12, such that  $E_1$  is the only barrier that contributes to the activation energy. Although for the case of xenon in the +2 charged supercell (red) the migration barriers are different, the same relative trends between barriers are predicted - i.e.  $w_2 \gg w_1$ . Therefore, the migration mechanism remains the same as for the neutral case and  $E_1$  plays the dominant role in governing migration.

The energy barriers for carbon vacancy mediated Kr migration in 3C-SiC are shown in Figure 8. As with Xe, the migration mechanism for Kr in the +2 charged supercell (red) is predicted to proceed through the rotation of a tightly bound vacancy-impurity pair where  $E_1$  contributes to the activation energy. However, in the neutral supercell (green)  $E_1 \approx E_2$  (at least within 0.04 eV) so that  $w_1 \approx w_2$ . In this case, the similar jump frequencies of impurity-vacancy exchange and rotation leads to a somewhat correlated motion, such that  $f \rightarrow \frac{1}{2}$  and  $E_2 \approx E_1$  contributes to the activation energy (equation 13).

Figure 9 shows the energy barriers associated with the five frequency model for I in the neutral supercell regime (green), indicating that  $E_1 > E_2$  or  $w_2 \gg w_1$ . In addition to the high binding energy, this reveals a migration mechanism that is again characterised by a tightly bound impurity-vacancy pair that rotates through the lattice. The diffusivity is, thus, determined by equation 12. Although the barriers are different, the same trends and mechanism are predicted for the +2 supercell (red).

In summary, nearly all of the cases studied exhibit a type b) migration mechanism (see section 2.2), whereby, the impurity rattles between the two carbon sites and the rotation of this tightly bound impurity-vacancy pair provides the means of diffusion. Kr in the neutral supercell exhibits some mixture of a) and b) type migration with a somewhat correlated diffusive motion. Based on these limiting cases the activation energies can be determined.

### 3.3. Activation energies

Table 3 summarises the activation energies for I, Xe and Kr for the neutral and +2 supercells calculated using equation 12 except for the case of Kr in the neutral supercell, where equation 13 is used. In the cases of the charged supercell the formation energy of the mediating carbon vacancy is dependent on the Fermi level,  $\mu_e$ , and, therefore, so is the activation energy. We have, thus, reported the activation energy as function of the Fermi level (see Table 3).

In line with previous simulations [20], it was predicted in section 3.1 that the transition between +2 and neutral carbon vacancies occurs at  $\mu_e = 1.33$  eV (see Figure 3). This indicated that the +2 regime is expected to dominate except for Fermi levels near the conduction band. Thus, one may promote high activation energies by favouring n-type doping, so long as one does not raise the Fermi level too near to the conduction edge where neutral vacancies begin to dominate. In the p-doping regimes (i.e. near the valence edge) the activation energy is lowest in part due to the low formation energy of the migration mediating carbon vacancies.

Xe has a higher activation energy than Kr across the entire band gap. Due to their similar inert chemistry this difference can be attributed to size effects. In the +2 regime it can be seen that, although the impurity-vacancy exchange barrier ( $E_2$ ) is lower for Xe, the diffusion limiting impurity-vacancy rotation barrier ( $E_1$ ) is in fact 0.46 eV lower for Kr. This is sufficient to ensure Kr has a lower activation energy in the +2 supercell despite the tighter binding ( $E_4 - E_3$ ) for Xe. In the neutral supercell Kr has a more attractive binding energy in addition to a lower rate limiting diffusion barrier, thus, contributing an even lower Kr activation energy compared to that of Xe. These results indicate that Kr will diffuse more rapidly than Xe regardless of the Fermi level.

Over the majority of the band gap (+2 regime) I exhibits the highest activation energy, indicating that it will diffuse more slowly than the noble gases. Early results from experimental studies reflect this, in that I has been observed to be immobile in SiC up to 1400 °C using SIMS characterisation [51], whereas, Xe exhibits limited mobility at 1350-1400 °C in thermal desorption experiments [52]. However, Figure 10 indicates that near the theoretical conduction edge it is possible that iodine mobility could exceed that of Xe. This is a consequence of the reduced  $E_1$  barrier for I in the neutral cell compared to the +2 supercell, whereas, the converse is true for the noble gases (see Table 2). This highlights a key way in which the chemistry of a given species affects mobility as function of the Fermi level and indicates how doping can manipulate the efficacy of SiC for fission product retention. These results should be checked by further experiments with controlled conditions, such as doping and stoichiometry.

#### 4. Conclusions

Density functional theory has been applied to investigate the vacancy-assisted migration of fission products in 3C-SiC. Based on the stability of carbon vacancies, the accommodation of fission products on the carbon sublattice and the metastability of the silicon vacancy, a justification is made for treating diffusion as limited to the FCC carbon sublattice. Furthermore, the +2 and neutral charge states are sufficient to describe the defects involved over the full theoretical band gap, with similar trends predicted by GW methods that give a more accurate theoretical band gap [25]. All migration barriers involved in the five frequency model have been calculated for Xe, Kr and I in the +2 and neutral supercells.

Results indicate that over the majority of the band gap the activation energy for I exceeds that of Xe which exceeds that of Kr. It is expected therefore that SiC is most effective at preventing I mobility, as supported by preliminary experimental results [51, 52]. Near the theoretical conduction edge the neutral case dominates and Xe exhibits the highest activation energy.

The activation energy for all species increases as a function of the Fermi level, indicating that n-type doping could be used to enhance the fission product retention properties of SiC. Raising the Fermi level reduces the stability carbon vacancies, thus, limiting their availability for assisting migration.

Further work should be done to investigate the attempt frequencies involved in the five frequency model for a full description of fission product diffusivity and models that incorporate more mechanisms involving longer range interactions must also be studied. Additionally, a more accurate description of defect energies over the full experimental band gap should be undertaken using hybrid functionals.

#### Acknowledgements

R.W. Grimes of Imperial College London, E. Vathonne of CEA Cadarache and D. A. Andersson from LANL are all acknowledged for useful discussion. Part of this work was performed using HPC resources from GENCI (grant t2013086922).

## References

- [1] M. Willander, M. Friesel, Q. U. Wahab, and B. Straumal, Silicon carbide and diamond for high temperature device applications, *J. Mater. Sci. Mater. Electron.* **17** (2006) 1–25.
- [2] L. Giancarli, M. Ferrari, M. A. Fütterer, and S. Malang, Candidate blanket concepts for a European fusion power plant study, *Fusion Eng. Des.* **49-50** (2000) 445–456.
- [3] P. Yvon and F. Carré, Structural materials for advanced reactor systems, *J. Nucl. Mater.* **385** (2009) 217–222.
- [4] A. W. Mehner, W. Heit, K. Röllig, H. Ragoss and H. Müller, Spherical fuel elements for advanced HTR manufacture and qualification by irradiation testing, *J. Nucl. Mater.* **171** (1990) 9–18.
- [5] A. N. Shirsat, M. Ali (Basu), S. Kolay, A. Datta and D. Das, Transport properties of I, Te and Xe in thoria-urania SIMFUEL, *J. Nucl. Mater.* **392** (2009) 16–21.
- [6] Y. Yun, P. M. Oppeneer, H. Kim and K. Park, Defect energetics and Xe diffusion in  $\text{UO}_2$  and  $\text{ThO}_2$ , *Acta Mater.* **57** (2009) 1655–1659.
- [7] J. A. Turnbull and C. A. Friskney, The diffusion coefficients of gaseous and volatile species during the irradiation of uranium dioxide, *J. Nucl. Mater.* **107** (1982) 168–184.
- [8] R. G. J. Ball and R. W. Grimes, Diffusion of Xe in  $\text{UO}_2$ , *J. Chem. Soc. Faraday Trans.* **86** (1990) 1257–1261.
- [9] H. J. Matzke, Gas release mechanisms in  $\text{UO}_2$  - a critical review, *Radiat. Eff.* **53** (1980) 219–242.
- [10] D. A. Andersson, P. Garcia, X.-Y. Liu, G. Pastore, M. Tonks, P. Millett, B. Dorado, D. R. Gaston, D. Andrs, R. L. Williamson, R. C. Martineau, B. P. Uberuaga and C. R. Stanek, Atomistic modeling of intrinsic and radiation enhanced fission gas (Xe) diffusion in  $\text{UO}_{2\pm x}$ : Implications for nuclear fuel performance modeling, *J. Nucl. Mater.* **451** (2014) 225–242.
- [11] R. W. Grimes, R. G. J. Ball and C. R. A. Catlow, Site preference and binding of iodine and caesium in uranium dioxide, *J. Phys. Chem. A* **53** (1992) 475–484.
- [12] R. G. J. Ball, W. G. Burns, J. Henshaw, M. A. Mignanelli and P. E. Potter, The chemical constitution of the fuel-clad gap in oxide fuel pins for nuclear reactors, *J. Nucl. Mater.* **167** (1989) 191–204.
- [13] K. Minato, T. Ogawa, S. Kashimura and K. Fukuda, Fission product palladium-silicon carbon interaction in HTGR fuel particles, *J. Nucl. Mater.* **172** (1990) 184–196.
- [14] L. Vincent, T. Sauvage, G. Carlot, P. Garcia, G. Martin, M. F. Barthe and P. Desgardin, Thermal behaviour of helium in silicon carbide: Influence of microstructure, *Vacuum* **83** (2009) 36–39.

- [15] K. Minato, T. Ogawa, K. Fukuda, M. Shimizu, Y. Tayama and I. Takahashi, Fission product behaviour in Triso-coated UO<sub>2</sub> fuel particles, *J. Nucl. Mater.* **208** (1994) 266–281.
- [16] D. A. Petti, J. Buongiorno, J. T. Maki, G. K. Miller and R. R. Hobbins, Key differences in the fabrication, irradiation and high temperature accident testing of US and German TRISO-coated particle fuel and their implications on fuel performance, *Nucl. Eng. Des.* **222(2-3 SPEC)** (2003) 281–297.
- [17] M. Bertolus, M. Freyss, B. Dorado, G. Martin, K. Hoang, S. Maillard, R. Skorek, P. Garcia, C. Valot, A. Chartier, L. Van Brutzel, P. Fossati, R. W. Grimes, D. C. Parfitt, C. L. Bishop, S. T. Murphy, M. J.D. Rushton, D. Staicu, E. Yakub, S. Nichenko, M. Krack, F. Devynck, R. Ngayam-Happy, K. Govers, C. S. Deo and R. K. Behera, Linking atomic and mesoscopic scales for the modelling of the transport properties of uranium dioxide under irradiation, *J. Nucl. Mater.* **462** (2015) 475–495.
- [18] J. Wiktor, M. Freyss, B. Amadon, M. Bertolus, G. Jomard and P. Garcia, Advances in first-principles modelling of point defects in UO<sub>2</sub>: f electron correlations and the issue of local energy minima, *J. Phys. Condens. Matter* **25** (2013) 333201.
- [19] X.-Y. Liu, D. A. Andersson and B. P. Uberuaga, First-principles DFT modeling of nuclear fuel materials, *J. Mater. Sci.* **47** (2012) 7367–7384.
- [20] J. Wiktor, G. Jomard, M. Torrent and M. Bertolus, Electronic structure investigation of energetics and positron lifetimes of fully relaxed monovacancies with various charge states in 3C-SiC and 6H-SiC, *Phys. Rev. B* **87** (2013) 235207.
- [21] M. Bertolus, *Modélisation à l'échelle atomique de matériaux nucléaires du cycle du combustible*, Technical report CEA-R-6281 (2011).
- [22] F. Gao, E. J. Bylaska, W. J. Weber and L. R. Corrales, Native defect properties in  $\beta$ -SiC: *Ab initio* and empirical potential calculations, *Nucl. Inst. Meth. Phys. Res. B* **180** (2001) 286–292.
- [23] C. Wang, J. Bernholc and R. F. Davis, Formation energies, abundances, and the electronic structure of native defects in cubic SiC, *Phys. Rev. B* **38** (1988) 12752.
- [24] F. Gao, E. J. Bylaska, W. J. Weber and L. R. Corrales, *Ab initio* and empirical-potential studies of defect properties in 3C-SiC, *Phys. Rev. B* **64** (2001) 245208.
- [25] F. Bruneval, Methodological aspect of the GW calculation of the carbon vacancy in 3C-SiC, *Nucl. Instruments Methods Phys. Res. Sect. B Beam Interact. with Mater. Atoms* **277** (2012) 77–79.
- [26] F. Bruneval and G. Roma, Energetics and metastability of the silicon vacancy in cubic SiC, *Phys. Rev. B* **83** (2011) 144116.
- [27] P. Deák, B. Aradi, T. Frauenheim, E. Jánzén and A. Gali, Accurate defect levels obtained from the HSE06 range-separated hybrid functional, *Phys. Rev. B* **81** (2010) 153203.
- [28] J. Rabone and A. Kovács, A DFT investigation of the interactions of Pd, Ag, Sn, and Cs with silicon carbide, *Int. J. Quant. Chem* **114** (2014) 1534–1545.
- [29] A. Charaf-Eddin and L. Pizzagalli, First principles calculation of noble gas atoms in 3C-SiC, *J. Nucl. Mater.* **429** (2012) 329–332.

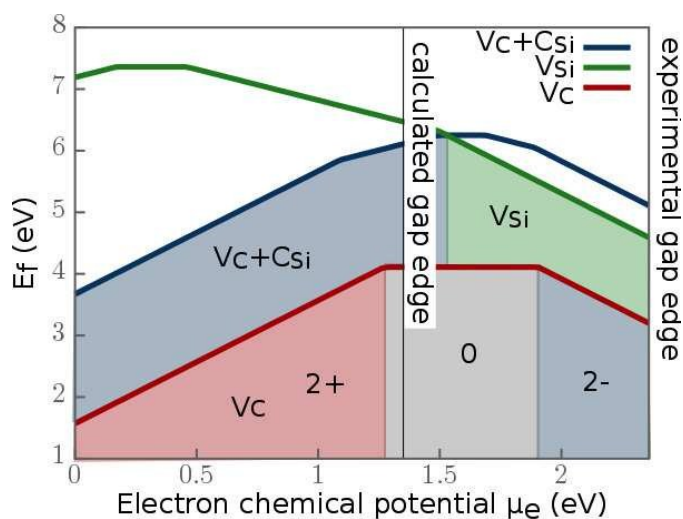
- [30] G. Roma, Palladium in cubic silicon carbide: stability and kinetics, *J. Appl. Phys.* **106** (2009) 123504.
- [31] D. Shrader, S. M. Khalil, T. Gerczak, T. R. Allen, A. J. Heim, I. Szlufarska and D. Morgan, Ag diffusion in cubic silicon carbide, *J. Nucl. Mater.* **408** (2011) 257-271.
- [32] V. Ivády, A. Gällström, N. T. Son, E. Janzén and A. Gali, Asymmetric split-vacancy defects in SiC polytypes: A combined theoretical and electronic spin resonance study, *Phys. Rev. Lett.* **107** (2011) 195501.
- [33] M. Bockstedte, A. Mattausch and O. Pankratov, *Ab initio* study of the migration of intrinsic defects in 3C-SiC, *Phys. Rev. B* **68** (2003) 205201.
- [34] N. T. Son, P. Carlsson, J. ul Hassa, E. Janzén, T. Umeda, J. Isoya, A Gali, M. Boskstedte, N. Morishita, T. Ohshima and H. Ito, Divacancy in 4H-SiC, *Phys. Rev. Lett.* **96** (2006) 055501.
- [35] P. E. Blöchl, Projector augmented-wave method, *Phys. Rev. B* **50** (1994) 17953-17979.
- [36] G. Kresse and D. Joubert, From ultrasoft pseudopotentials to the projector augmented-wave method, *Phys. Rev. B* **59** (1999) 1758-1775.
- [37] G. Kresse and J. Hafner, *Ab initio* molecular dynamics for liquid metals, *Phys. Rev. B* **47** (1993) 558-561.
- [38] G. Kresse and J. Hafner, *Ab initio* molecular dynamics of the liquid-metal-amorphous-semiconductor transition in germanium, *Phys. Rev. B* **49** (1994) 14251-14269.
- [39] G. Kresse and J. Furthmüller, Efficiency of *ab initio* total energy calculations for metals and semiconductors using a plane-wave basis set, *Comput. Mater. Sci.* **6** (1996) 15-50.
- [40] J. P. Perdew, K. Burke and M. Ernzerhof, Generalized gradient approximation made simple, *Phys. Rev. Lett.* **77** (1996) 3865-3868.
- [41] H. J. Monkhorst and J. D. Pack, Special points for Brillouin-zone integrations, *Phys. Rev. B* **13** (1976) 1748-1749.
- [42] M. Leslie and N. J. Gillan, The energy and elastic dipole tensor of defects in ionic crystals calculated by the supercell method, *J. Phys. C: Solid State Phys.* **18** (1985) 973-982.
- [43] G. Makov and M. C. Payne, Periodic boundary conditions in *ab initio* calculations, *Phys. Rev. B* **51** (1995) 4014-4022.
- [44] S. T. Murphy and N. D. M. Hine, Anisotropic charge screening and supercell size convergence of defect formation energies, *Phys. Rev. B* **87** (2013) 094111.
- [45] S. E. Taylor and F. Bruneval, Understanding and correcting spurious interactions in charged supercells, *Phys. Rev. B* **84** (2011) 075155.
- [46] G. Henkelman, B. P. Uberuaga and J. Hine, A climbing image nudged elastic band method for finding saddle points and minimum energy paths, *J. Chem. Phys.* **113** (2000) 9901.
- [47] G. Lucas and L. Pizzagalli, Theoretical study of the recombination of Frenkel pairs in irradiated silicon carbide, *J. Phys.: Condens. Matter* **19** (2007) 086208.

- [48] J. Manning, Correlation factors for impurity diffusion. bcc, diamond, and fcc structures, *Phys. Rev.* **136** (1964) 1758–1766.
- [49] H. Mehrer (2007) *Diffusion in Solids*, Springer-Verlag Berlin Heidelberg.
- [50] M. Bockstedte, A. Mattausch and O. Pankratov, *Ab initio* study of the annealing of vacancies and interstitials in cubic SiC: Vacancy-interstitial recombination and aggregation of carbon interstitials, *Phys. Rev. B* **69** (2004) 235202.
- [51] G. Carlot, private communication.
- [52] E. Gilabert (2012) GdR MATINEX plenary meeting.
- [53] D. H. Lee and J. D. Joannopoulos, Simple scheme for deriving atomic force constants: Application to SiC, *Phys. Rev. Lett.* **48** (1982) 1846.
- [54] W. J. Choyke, D. R. Hamilton and L. Patrick, optical properties of cubic SiC: luminescence of nitrogen-exciton complexes, and interband absorption, *Phys. Rev.* **133** (1964) 1163–1166.
- [55] L. Patrick and W. J. Choyke, Static dielectric constant of SiC, *Phys. Rev. B* **2** (1970) 2255–2256.

## Figures and Tables

**Table 1:** The bulk properties of 3C-SiC predicted using the DFT method in this work and from previous experimental work [53–55].

	DFT (present work)	Experimental
Lattice parameter	4.379 Å	4.36 Å [53]
Band gap	1.38 eV	2.39 eV [54]
Static dielectric constant, $\epsilon_s$	9.72	9.72 [55]

**Figure 1:** The formation energy for the carbon vacancy, a carbon vacancy  $C_{Si}$  antisite pair and a silicon vacancy as a function of the Fermi level. Values are reported up to the experimental band gap limit of 2.39 eV. The calculated band gap limit of 1.38 eV is shown by the dotted line. Data for Figure taken in reference [20].

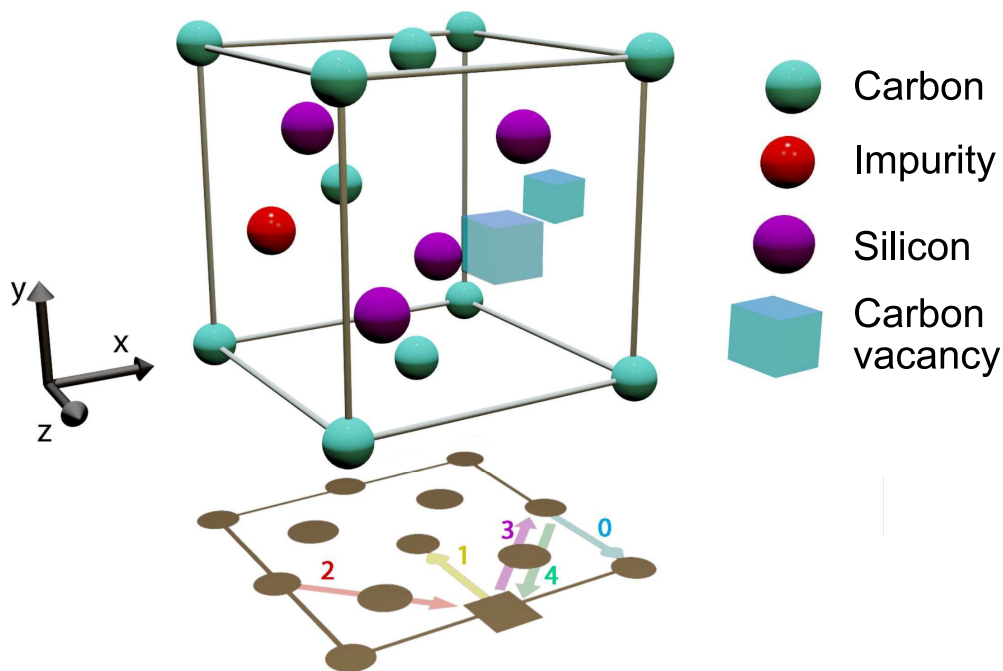


**Figure 2:** The jumps involved in the five frequency model are indicated using coloured arrows: i)  $w_0$  (blue) - vacancy migration in the bulk (beyond the first nearest neighbour), ii)  $w_1$  (yellow) - vacancy migration between two first nearest sites with respect to the impurity, iii)  $w_2$  (red) - the migration of the impurity into the vacancy, iv)  $w_3$  (purple) - vacancy migration from the first nearest neighbour site to the second nearest neighbour site, v)  $w_4$  (green) - vacancy migration from the second nearest neighbour site to the first nearest neighbour site. Silicon and carbon are represented by purple and turquoise spheres respectively. The red sphere indicates the impurity atom (Xe, Kr or I).

**Table 2:** The energy barriers for Xe, Kr and I associated with the jump frequencies of the five-frequency model, as shown in Figure 2. Values are reported for the charge neutral and +2 supercells. Note that  $E_B = E_4 - E_3$ .

Label	Reaction	Neutral				Charged +2			
		V <sub>C</sub>	Xe	Kr	I	V <sub>C</sub>	Xe	Kr	I
$E_0$	Host vacancy-atom exchange	3.42	-	-	-	5.54	-	-	-
$E_1$	Impurity-vacancy rotation	-	4.01	3.30	3.55	-	3.64	3.18	3.96
$E_2$	Impurity-vacancy exchange	-	3.87	3.34	3.00	-	2.68	2.69	3.63
$E_3$	Impurity-vacancy dissociation	-	5.32	3.81	4.24	-	4.58	4.63	4.63
$E_4$	Impurity-vacancy association	-	2.65	0.97	1.23	-	3.02	3.17	3.75

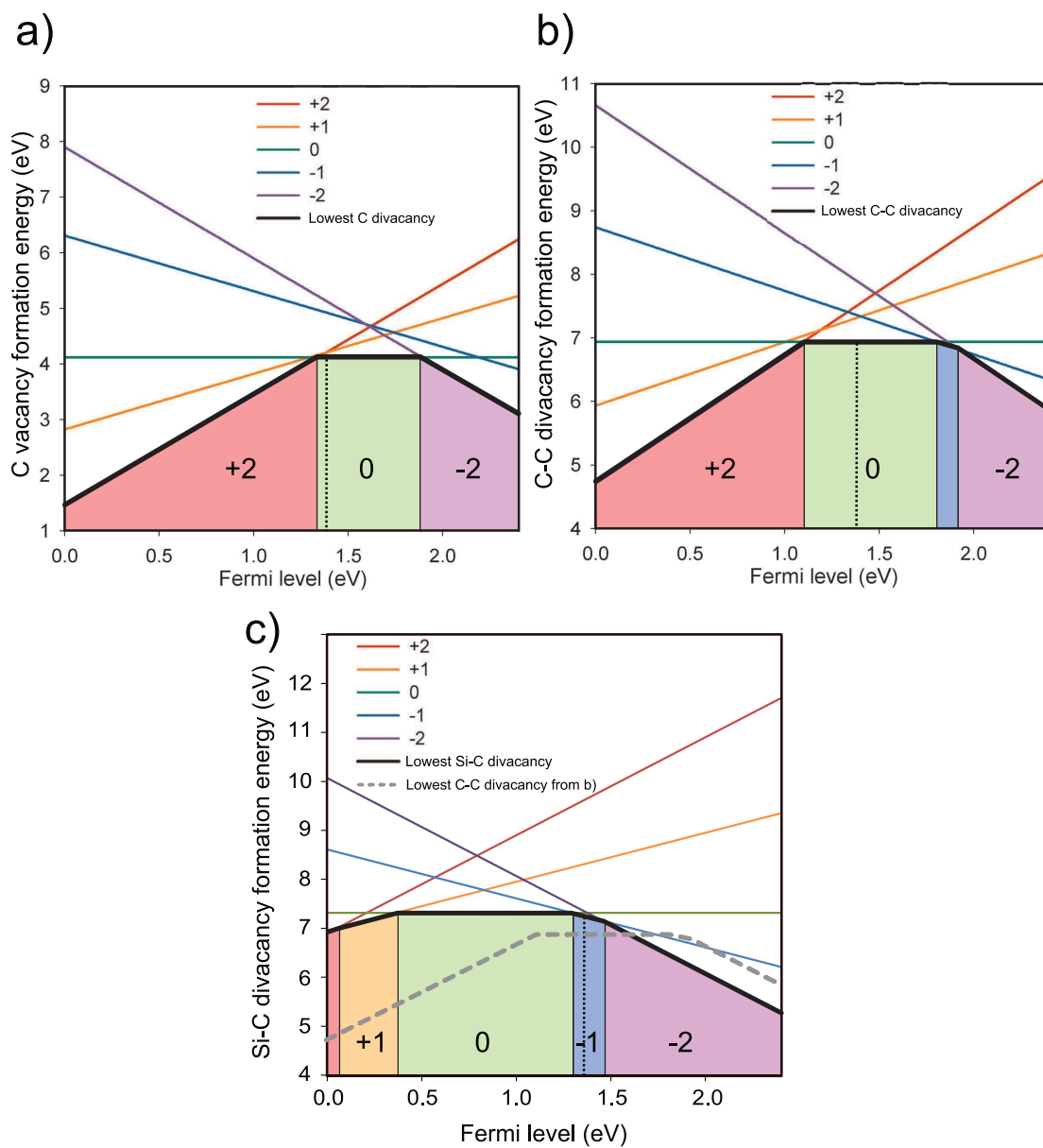


**Figure 3:** The formation energy for a) the carbon vacancy, b) carbon-carbon divacancy and c) silicon-carbon divacancy as a function of the Fermi level. Values are reported up to the experimental band gap limit of 2.39 eV. The calculated band gap limit of 1.38 eV is shown by the vertical dotted line.

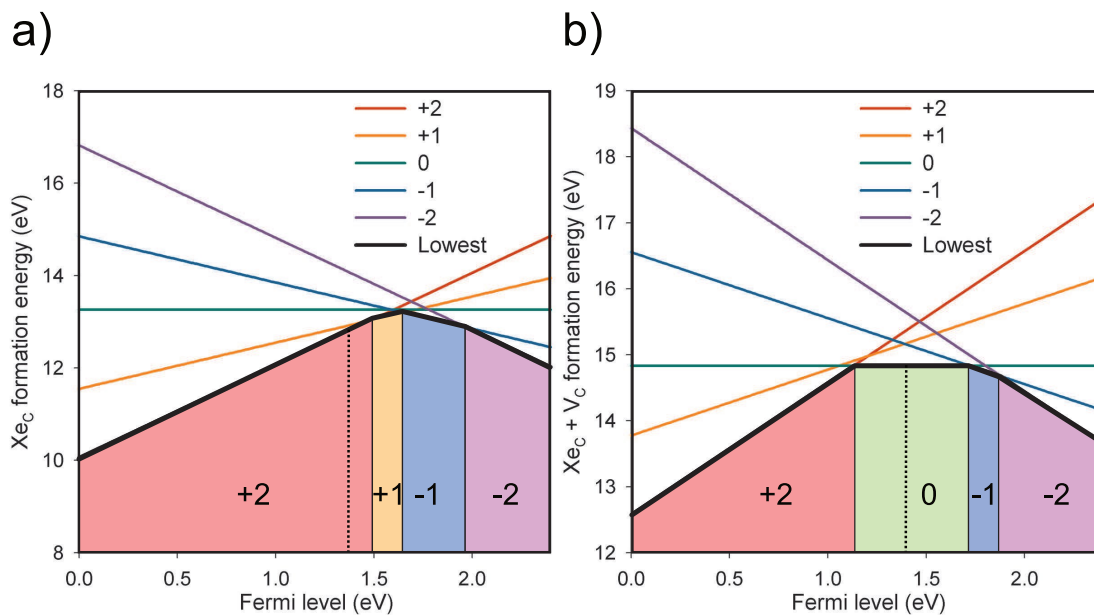


**Figure 4:** The formation energy for the accommodation of Xe at a) the carbon vacancy and b) carbon-carbon divacancy as a function of the Fermi level. Values are reported up to the experimental band gap limit of 2.39 eV. The calculated band gap limit of 1.38 eV is shown by the dotted line.

**Table 3:** The activation energy for I Kr and Xe in the charge neutral and 2+ supercells. These activation energies are also reported in Figure 10.

Impurity	Neutral	Charged +2
Xe	$E_f + E_B + E_1 = 5.45$	$E_f + E_B + E_1 = 3.29 + 2\mu_e$
Kr	$E_f + E_B + E_{1=2} = 4.60$	$E_f + E_B + E_1 = 2.92 + 2\mu_e$
I	$E_f + E_B + E_1 = 4.65$	$E_f + E_B + E_1 = 4.27 + 2\mu_e$

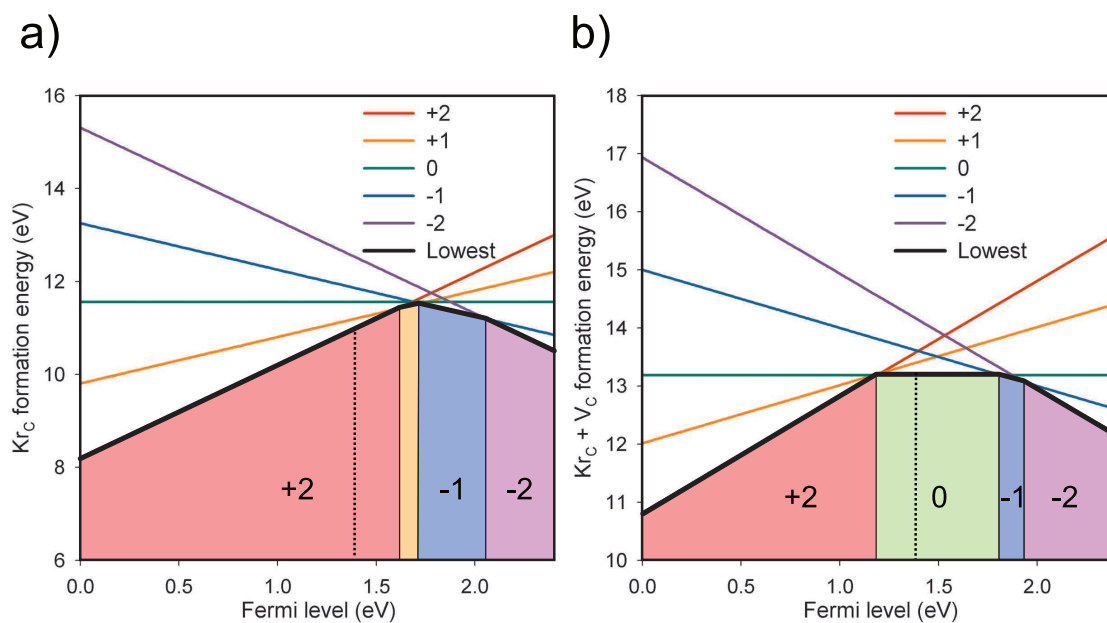


**Figure 5:** The formation energy for the accommodation of Kr at a) the carbon vacancy and b) carbon-carbon divacancy as a function of the Fermi level. Values are reported up to the experimental band gap limit of 2.39 eV. The calculated band gap limit of 1.38 eV is shown by the dotted line.

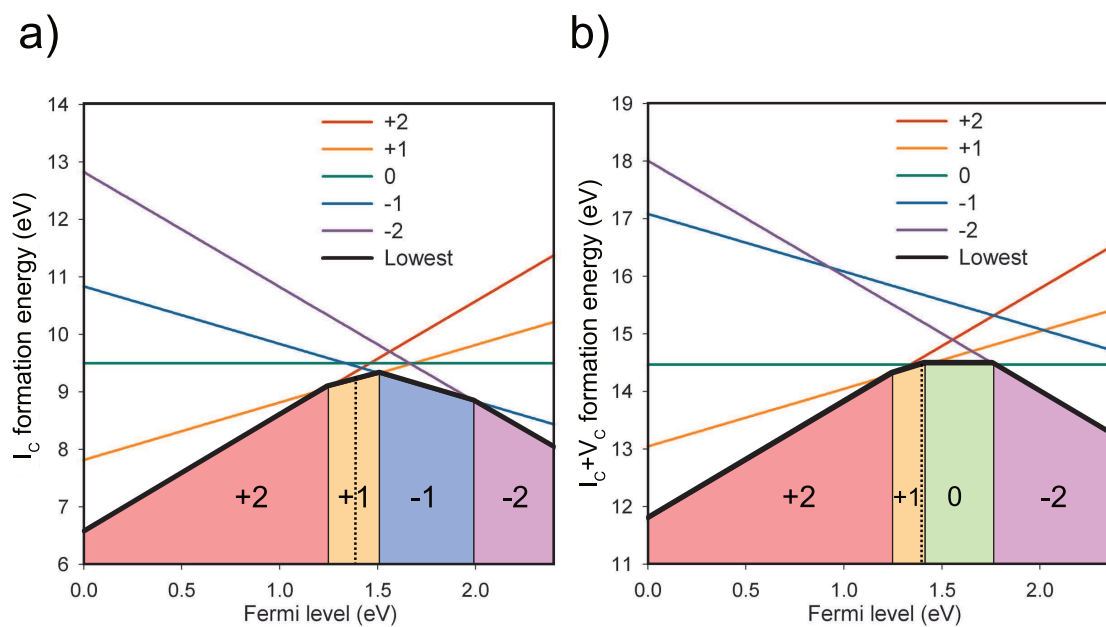


**Figure 6:** The formation energy for the accommodation of I at a) the carbon vacancy and b) carbon-carbon divacancy as a function of the Fermi level. Values are reported up to the experimental band gap limit of 2.39 eV. The calculated band gap limit of 1.38 eV is shown by the dotted line.

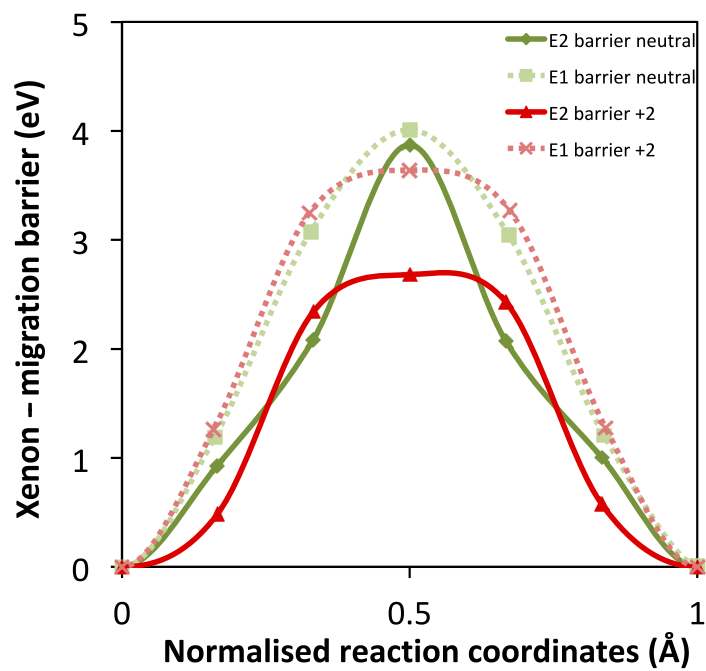


**Figure 7:** The migration barrier for the impurity-vacancy exchange rate ( $E_2$ ) and rotation rate ( $E_1$ ) for Xe in a charge neutral (green) and a +2 supercell (red).

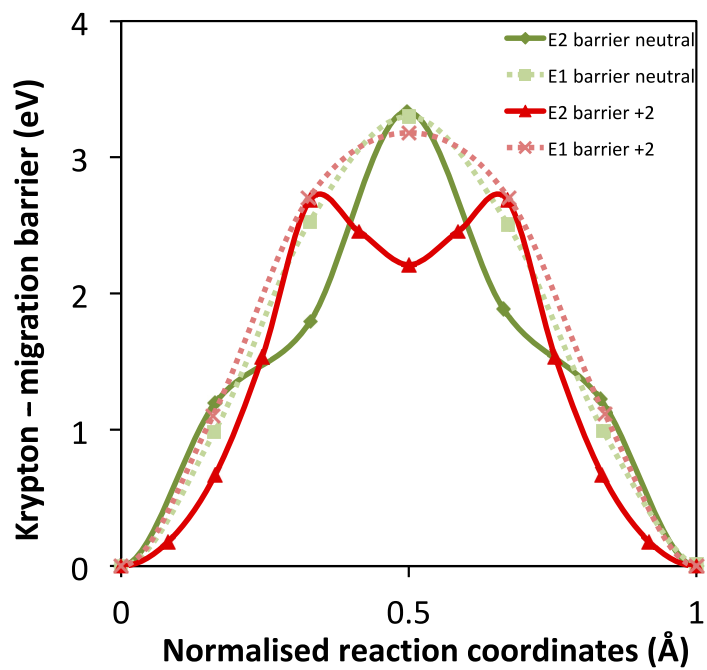


**Figure 8:** The migration barrier for the impurity-vacancy exchange rate ( $E_2$ ) and rotation rate ( $E_1$ ) for Kr in a charge neutral (green) and a +2 supercell (red).

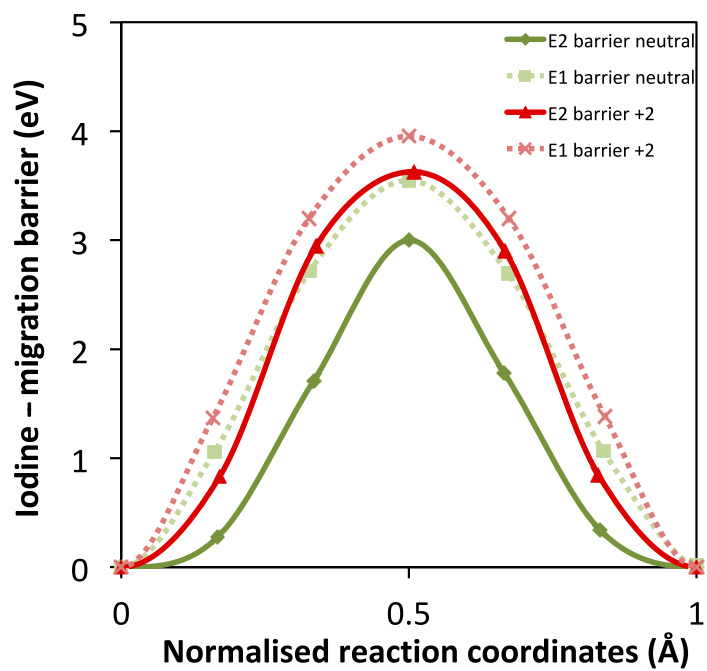


**Figure 9:** The migration barrier for the impurity-vacancy exchange rate ( $E_2$ ) and rotation rate ( $E_1$ ) for I in a charge neutral (green) and a +2 supercell (red).

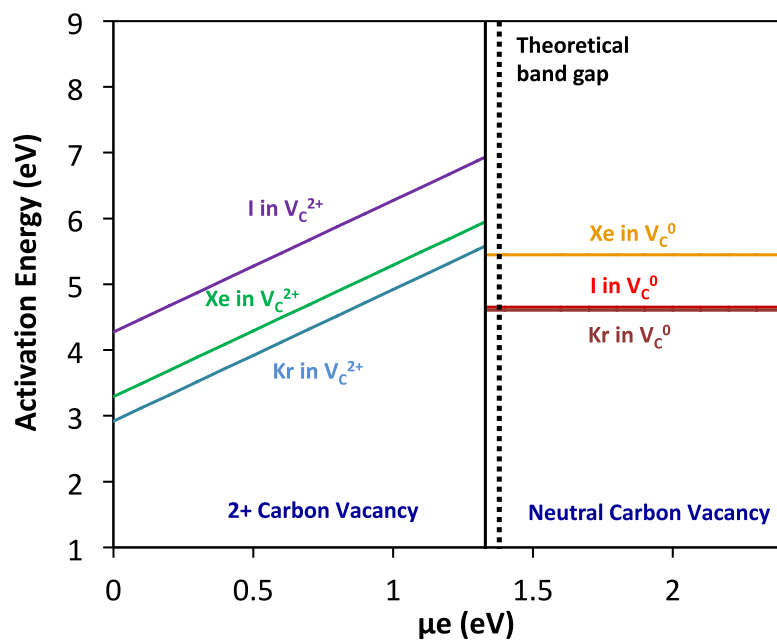


**Figure 10:** The activation energy for Xe, Kr and I as a function of the Fermi level. The Fermi level below which charge carbon vacancies are dominant is identified by a vertical black line. The range of values are dictated by the experimental band gap of 2.39 eV and the energy below which +2 carbon vacancies are more favourable is shown by the black line. The calculated band gap limit of 1.38 eV is shown by the dotted line.